Performance evaluation of polycrystalline HgI₂ photoconductors for radiation therapy imaging

Qihua Zhao,[a] Larry E. Antonuk, Youcef El-Mohri, Yi Wang,[b] Hong Du,[c] Amit Sawant,[d] Zhong Su,[e] and Jin Yamamoto[f]
Department of Radiation Oncology, University of Michigan, Ann Arbor, Michigan 48019

Purpose: Electronic portal imaging devices based on megavoltage (MV), active matrix, flat-panel imagers (AMFPIs) are presently regarded as the gold standard in portal imaging for external beam radiation therapy. These devices, employing indirect detection of incident radiation by means of a metal plate plus phosphor screen combination, offer a quantum efficiency of only ~2% at 6 MV, leading to a detective quantum efficiency (DQE) of only ~1%. In order to significantly improve the DQE performance of MV AMFPIs, a strategy based on the development of direct detection imagers incorporating thick films of polycrystalline mercuric iodide (HgI₂) photoconductor was undertaken and is reported.
Methods: Two MV AMFPI prototypes, one incorporating an ~300 μm thick HgI₂ layer created through physical vapor deposition (PVD) and a second incorporating an ~460 μm thick HgI₂ layer created through screen-printing of particle-in-binder (PIB) material, were quantitatively evaluated using a 6 MV photon beam. The reported measurements include empirical determination of x-ray sensitivity, lag, modulation transfer function (MTF), noise power spectrum, and DQE.
Results: For both prototypes, MTF and DQE results were found to be consistent with theoretical expectations and the MTFs were also found to be higher than that measured from a conventional MV AMFPI. In addition, the DQE results exhibit input-quantum-limited behavior, even at extremely low doses. Compared to PVD, the PIB prototype exhibits much lower dark current, slightly higher lag, and similar DQE. Finally, the challenges associated with this approach, as well as strategies for achieving considerably higher DQE through thicker HgI₂ layers, are discussed.
Conclusions: The DQE of each of the prototypes is found to be comparable to that of conventional MV AMFPIs, commensurate with the modest photoconductor thicknesses of these early samples. It is anticipated that thicker layers of HgI₂ based on PIB deposition can provide higher DQE while maintaining good material properties. © *2010 American Association of Physicists in Medicine.*
[DOI: 10.1118/1.3416924]

Key words: megavoltage x-ray imaging, flat-panel imager, EPID, DQE, polycrystalline mercuric iodide, PVD, PIB

I. INTRODUCTION

A central goal of external beam radiation therapy is to deliver maximum dose to the tumor while minimizing the dose delivered to surrounding normal tissues. To assist in this goal, portal imaging with film cassettes has long been employed for patient setup verification.[1] Recently, electronic portal imaging devices (EPIDs) have become widely used due to their significant advantages over film.[2–4] Contemporary EPID technology is primarily based on megavoltage (MV), active matrix, flat-panel imagers (AMFPIs) employing indirect detection of incident radiation by means of a metal plate and a phosphor screen combination of the type used in portal film cassettes.[4–7] These MV AMFPIs (referred to as *conventional* MV AMFPIs in this article) offer numerous advantages such as improved detective quantum efficiency (DQE) and image quality, as well as digital image format and instant image display,[3,4,6] and are presently regarded as the gold standard in portal imaging.[4,8] An alternative form of MV AMFPI, employing an a-Se photoconductor

for direct detection of incident radiation, has been investigated but has not been clinically implemented.[9–12]

Despite their advantages, conventional MV AMFPIs offer only a very low quantum efficiency (QE) of ~2% at 6 MV. This is a consequence of the limited x-ray attenuation of the x-ray detector at megavoltage energies. Such detectors typically consist of an ~1 mm thick Cu plate and a $Gd_2O_2S:Tb$ screen with a surface density of ~133 mg/cm².[4,6,13] Such low QE leads to a maximum DQE of only ~1%.[4,7,13,14] By comparison, AMFPIs designed for diagnostic applications typically exhibit maximum DQE values in the range of 40%–80%.[15–17] It is anticipated that improvements in DQE for MV AMFPIs should lead to significantly improved imaging performance, reduced dose, and soft-tissue visualization by means of MV cone beam computed tomography performed at clinically acceptable doses.[18–20]

Since the performance of conventional MV AMFPIs is already x-ray input-quantum-limited,[13,14] improving the DQE of such systems requires an increase in the QE of the x-ray detector. Unfortunately, increasing QE by simply em-

ploying thicker phosphor screens diminishes spatial resolution[21] and increases optical Swank noise,[22] both of which degrade DQE performance. In order to achieve significantly improved DQE performance from MV AMFPIs, as well as from other forms of EPIDs, a variety of high QE detectors have been investigated. For example, the use of linear arrays of detectors scanned across the field of view has been explored with detector configurations such as a 25 mm thick segmented ZnWO$_4$ scintillator,[23] a 25 mm thick segmented CsI:Tl scintillator,[24] and a 2 mm thick CdTe detector.[25] Other linear detector array concepts include a segmented BGO scintillator and a CdWO$_4$ scintillator for MV computed tomography,[26,27] a xenon gas ionization chamber for tomotherapy,[28] and a 100 atm xenon gas detector incorporated in a kinestatic charge detection EPID.[29,30] In addition, 2D detectors that have been investigated include a 12 mm thick CsI:Tl scintillator coupled to a video camera,[31] a 10 mm thick segmented CsI:Tl scintillator coupled to a lens and CCD camera,[32,33] a Cerenkov radiation detection EPID incorporating an ~30 cm thick taper consisting of a matrix of optical fibers,[34] and a xenon gas detector with tungsten walls consisting of microstructured plates packed together and aligned with the incident x-ray beam.[35] Furthermore, 2D scintillators integrated into MV AMFPIs include a 0.8 mm thick CsI:Tl needle scintillator,[36] a 2 mm thick segmented phosphor scintillator,[22] and several segmented CsI:Tl and BGO scintillators with thicknesses ranging from 8 to 40 mm.[18,19,37,38]

An alternative approach for improving DQE performance involves the development of direct detection MV AMFPIs incorporating thick films of polycrystalline mercuric iodide (HgI$_2$) photoconductor. In direct detection AMFPIs, the charge created by x-ray interactions within the photoconductor is collected by means of an externally applied electric field, resulting in minimal lateral spread of the imaging signal. This characteristic means that, in principle, photoconductor thickness (and QE) can be increased without serious degradation of spatial resolution, other than that due to obliquely incident radiation. Compared to detector materials used in conventional diagnostic or MV AMFPIs (i.e., Gd$_2$O$_2$S:Tb, CsI:Tl, and a-Se), HgI$_2$ exhibits a higher effective atomic number (Z_{eff}, 66) and a relatively high material density (ρ, 6.36 g/cm^3), which result in a high x-ray attenuation. By comparison, for Gd$_2$O$_2$S:Tb phosphor screens, CsI:Tl and a-Se, Z_{eff} is 57 (ignoring binder material), 54, and 34, while ρ is ~3.7, 4.5, and 4.3 g/cm^3, respectively. In addition, relatively thick layers of HgI$_2$ are conceivable, as suggested by an early study of polycrystalline HgI$_2$ samples as thick as 1.8 mm.[39] Finally, the electric field strength required to extract signal from polycrystalline HgI$_2$ at high levels of sensitivity is only on the order of ~0.5 to 1 V/μm,[40–44] much lower than the ~10 V/μm required for a-Se detectors.[45]

In this article, an initial investigation of the signal and noise properties of prototype MV AMFPIs incorporating polycrystalline HgI$_2$ is reported. The results include empirical determination of sensitivity, lag, modulation transfer

TABLE I. Specifications for the PIB and PVD MV AMFPI prototypes examined in this study.

Prototype	PIB	PVD
Barrier layer thickness	3 μm	~1.5 μm
Photoconductor thickness	460 μm	300 μm
Packing density	~50%	~90%
Quantum efficiency (at 6 MV)	~2.1%	~2.5%

function (MTF), noise power spectrum (NPS), and DQE. Sensitivity, MTF, and DQE results are compared to those obtained from a conventional MV AMFPI, as well as with theoretical calculations based on Monte Carlo simulations. While these early prototypes employ relatively thin layers of HgI$_2$ (providing QE only comparable to that of the Gd$_2$O$_2$S:Tb detectors used in conventional MV AMFPIs), the study was conducted in the spirit of acquiring the experience necessary to develop thicker, higher QE HgI$_2$ detectors in the future. Finally, the challenges inherent in this approach, strategies for meeting these challenges, and prospects for further progress are discussed.

II. METHODS AND MATERIALS

II.A. Prototype imagers

Two MV AMFPI prototypes were examined in this study. Each prototype consists of a layer of polycrystalline HgI$_2$ photoconductor coated on an AMFPI array, using a screen-printing technique with particle-in-binder (PIB) material for one prototype and a physical vapor deposition (PVD) method for the other.[46,47] Specifications for the PIB and PVD prototypes, referred to as PIB#1 and PVD#2 in a previous publication,[43] are listed in Table I. The PIB layer is ~460 μm thick and consists of HgI$_2$ grains mixed with a polymer binder (having a mass density of 1.05 g/cm^3). The packing density (defined as the mass density of the HgI$_2$ layer expressed as a percentage of the single crystal density of this material) is ~50%. The PVD layer is ~300 μm thick with a packing density of ~90%. Figure 1 shows photomicrographs of the surface of the HgI$_2$ layer for the two prototypes, illustrating significant differences due to their respective compositions and fabrication techniques.

In the previous study involving these and 18 other PIB and PVD prototypes,[43] a variety of properties (i.e., charge trapping, lag, pixel response, linearity, uniformity of pixel response, x-ray sensitivity, effective work function, MTF and, for one PVD prototype, NPS and DQE) were investigated under diagnostic irradiation conditions (72 kVp, 20 mm Al filtration). However, neither the properties of any of these 20 prototypes, nor of any other similarly coated arrays, have been previously investigated under MV irradiation conditions. Furthermore, the considerably different energy spectrum of a MV beam (resulting in a much more uniform deposition of energy across the detector thickness), as well as the very different temporal structure of the MV radiation beam (~5 μs beam pulses every ~16.7 ms), make it unlikely that properties determined under diagnostic conditions could be
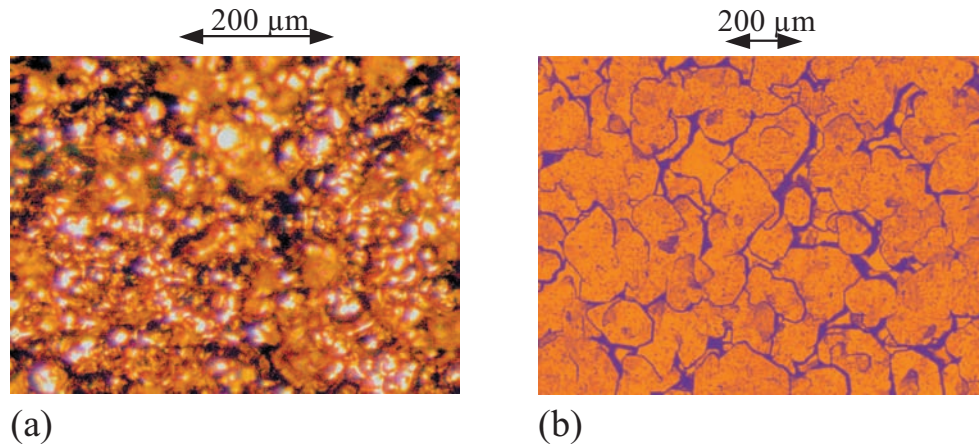
FIG. 1. Photomicrographs of the surface of the (a) PIB and (b) PVD polycrystalline HgI_2 photoconductor prototypes used in this study.

used to reliably predict those under MV conditions. While it has been previously suggested[43] that non-performance-related considerations may favor the PIB form of the material for MV imaging (namely, comparative ease of fabrication for thick detectors, as further detailed in Sec. IV of this article), the above considerations make it interesting and sensible to perform an objective examination of prototypes based on both PIB and PVD. Also note that, while dark current and signal current results obtained under MV conditions from film detectors with barrier and polycrystalline HgI_2 layers similar to those of the present study have previously been reported,[44] the relatively simple construction of those detectors precludes acquisition of the type of spatial frequency-dependent information offered by arrays.

The AMFPI arrays used for the two prototypes are based on a direct detection design referred to as ND10 (dpiX, USA). ND10 has a pixel pitch of 127 μm and a pixel format of 768×768, providing an imaging area of ∼9.8×9.8 cm². Each pixel consists of an a-Si:H thin-film-transistor (TFT) and a storage capacitor. Figure 2 shows a schematic drawing of a cross-sectional view of a single array pixel. As shown in the figure, HgI_2 photoconductor was coated on top of a polymer-based barrier layer, which was applied to the array to prevent chemical damage by the HgI_2. The barrier layer also provides adhesion between the photoconductor and the array surface, while still allowing transport of x-ray induced charge from the photoconductor to the underlying electrodes.[43] An ∼1000 Å thick palladium layer, serving as a top electrode, was deposited directly on the photoconductor.

In addition, an ∼1 mm thick Cu plate, wrapped in a sheet of paper to avoid electrical contact with the top electrode, was placed over the HgI_2 to absorb scattered, low energy electrons and photons, as well as to increase quantum efficiency. The x-ray detector thus consists of the HgI_2 photoconductor and the Cu plate. Note that the choice of an ∼1 mm Cu plate in this study corresponds to that used in conventional MV AMFPIs as well as that used in an investigational MV AMFPI incorporating a-Se.[12] While adjust-

ment of the physical parameters of the plate could result in improvement in performance, this was beyond the scope of the present investigation.

During image acquisition, the pixel TFTs are kept non-conducting and imaging signal due to charge created in the HgI_2 material by interacting X rays is accumulated in the pixel storage capacitors. This signal is read out, one row of pixels at a time, by rendering the corresponding TFTs conducting, and then amplified and digitized by external electronics.

II.B. Measurement methods

The measurements were performed using a 6 MV photon beam delivered by a Varian 21EX linear accelerator (linac). Unless otherwise specified, the linac was operated at a dose rate of 100 monitor units (MUs) per minute with a field size of 10×10 cm². The linac is calibrated so that 1 MU corre-
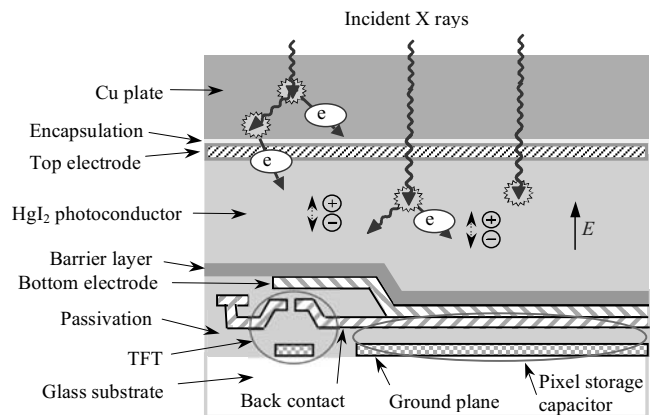

FIG. 2. Schematic, cross-sectional view of a portion of a prototype array pixel. The region depicted in the drawing corresponds to a single array pixel along with the various overlying layers associated with the x-ray detector. The ellipses superimposed on the drawing indicate the general region of the TFT and pixel storage capacitor. Note that the drawing is not to scale and, in particular, the dimensions of various features in the vertical direction have been exaggerated for clarity of presentation.

sponds to a dose of ∼0.8 cGy at a distance of 100 cm from the radiation source at a depth of 10 cm in water with a 10×10 cm^2 field. Each MU corresponds to the delivery of ∼36 beam pulses. A custom-designed data acquisition system, G3,[48] was employed to control array operation, including signal readout, amplification, digitization, and data transfer. In addition, a low noise ASIC chip, MASDA-R,[49] was used for signal preamplification. During acquisition, a *data frame* is formed through readout of the entire array. *Image frames* and *dark frames* correspond to data frames acquired with and without radiation, respectively. Signal and noise data, including sensitivity, lag, and NPS, were acquired in fluoroscopic mode, while MTF data were acquired in radiographic mode.[13,50,51]

In fluoroscopic mode, a sequence of image frames was acquired in synchronization with beam pulses (using the "Target I" signal provided by the linac), so that every image frame was read out after delivery of a predetermined number of pulses. Dark frames were acquired in synchronization with pulses generated by a pulse generator (33250A, Agilent Technologies, Inc., USA) operated at the same frequency as the beam pulses. In radiographic mode, an image frame was acquired after the delivery of preprogrammed MUs over a time interval set by the G3 system. A dark frame in this mode was acquired over the same time interval.

Dark and image frames were binned in a 4×4 format resulting in data frames with 192×192 "pixels" at a pixel pitch of 508 μm, matching that of a conventional MV AMFPI, results from which are reported for purposes of comparison. This conventional MV AMFPI consists of an indirect detection array with 512×512 pixels, a Lanex FAST B screen (360 μm of Gd$_2$O$_2$S:Tb with a packing density of ∼50%), and an ∼1 mm thick Cu plate.[13] The sensitivity, MTF, and DQE results measured from the prototypes are directly compared to those measured from the conventional MV AMFPI.

II.B.1. Selection of electric field strength

A negative bias voltage was applied to the top (palladium) electrode to provide an electric field across the photoconductor for efficient charge collection during the measurements. The strength of this electric field was selected through empirical investigation of the dependence of pixel signal response and dark current on the magnitude of this field, as described in Sec. III.

II.B.2. Measurement setup

In the signal and noise measurements, a source-to-detector distance (SDD) of 350 cm was chosen, unless otherwise indicated, to allow the investigation of prototype performance at very low doses. In order to permit this extended SDD, the gantry of the linac was positioned at 90° and the plane of the MV AMFPI prototype was oriented perpendicular to the floor. In addition, the prototypes were located far from walls to reduce contribution from backscatter radiation. With this arrangement, the x-ray signal of the prototypes, obtained from the average of dark-subtracted image frames,

was kept below ∼5% of pixel saturation, corresponding to operational conditions under which pixel signal response is highly linear. Given that the x-ray fluence (i.e., the number of X rays per unit area) at an SDD of 350 cm is only ∼13.8% of that at the typical distance that MV AMFPIs are positioned (130 cm),[37] an irradiation of 1 MU at 350 cm can be considered approximately equivalent to an irradiation 0.138 MU at 130 cm. Therefore, to convey the signal and noise performance to be expected at 130 cm, the doses for the reported sensitivity, lag, and NPS measurements and results for sensitivity have been adjusted by a factor of 0.138.

II.B.3. Sensitivity

In order to evaluate x-ray sensitivity, x-ray induced pixel signal was measured as a function of dose in units of MU. Several sequences of image frames were acquired with each sequence comprising 2, 4, 6, 8, 14, or 20 beam pulses per frame, corresponding to ∼0.008, 0.015, 0.023, 0.031, 0.054, and 0.077 MU, respectively. For each sequence, a set of 100 dark frames and a set of 100 image frames were acquired and averaged to produce a single dark frame and a single image frame, respectively — the difference of which yielded the pixel signal response. Sensitivity, in units of e/MU, was determined from the slope of a linear fit to the pixel signal response data plotted as a function of radiation dose.

II.B.4. Lag

Lag measurements were performed at a frame time T_F (defined as the time period between the beginning of consecutive frames) of ∼0.35 s. For each prototype, three sequences of data frames were acquired, each sequence consisting of an initial 30 dark frames, followed by 220 image frames (with a constant number of beam pulses per frame), and a final 150 dark frames. These image frames were acquired with 8, 12, or 20 beam pulses per frame, corresponding to ∼0.031, 0.046, and 0.077 MU, respectively. Further details about the determination of lag appear in Sec. III C.

II.B.5. MTF

The MTF was measured using the angled slit technique.[52] The slit consists of a pair of $20 \times 10 \times 5$ cm^3 steel blocks separated by 0.01 cm thick shims, resulting in a 0.01 cm gap, which is 5 cm long and 20 cm deep.[22] The linac gantry was positioned at 0° and the slit was mounted in the accessory slot of the linac and positioned such that the exit surface of the slit was almost in contact with the prototype, resulting in a SDD of ∼86 cm.

In these measurements, the slit gap was centered with respect to the radiation source in order to maximize the radiation transmitted through the gap. In addition, the slit gap was oriented at a small angle (∼1°) with respect to the data lines of the array to allow oversampling of the line spread function (LSF). For each prototype, five slit image frames were acquired at a dose rate of 600 MU/min. Five "radiation dark" frames were also acquired with the slit laterally dis-

placed ~0.6 cm from the centered position, using the same amount of radiation as in the acquisition of the slit images so as to provide a measure of the radiation penetrating through the blocks. The slit image frames and data radiation dark frames were processed through application of gain and offset corrections.[53] Subsequently, the slit image frames were corrected through subtraction of background radiation (using the averaged radiation dark data) and correction for defective pixels (using a 3×3 median filter). The processed slit images were averaged to produce LSF data, the Fourier transforms of which yielded presampled MTF results.

II.B.6. NPS and DQE

For both prototypes, dark and image frames acquired for the sensitivity study were also used to determine NPS. Gain and offset corrections were applied to the image frames, while only offset corrections were applied to the dark frames. Correction for defective pixels using the 3×3 median filter affected less than 0.2% of the total number of pixels per frame. NPS results were obtained from these frames using the synthesized slit technique,[13] with 100 independent, non-overlapping "slits" formed from the image frames for each prototype. Each slit consisted of data from a block of 151×72 pixels for the PIB prototype (144×96 pixels for the PVD prototype), with the longer dimension oriented along the gate line direction. For each slit, pixel data were summed along the data line direction to form a 151 (144) point realization for PIB (PVD). In addition, the low frequency background trend was subtracted and a Hanning window function was applied to each realization. A Fourier transform was then applied to each of the 100 realizations, resulting in a series of 1D NPS. The final empirical NPS was determined from the average of these 1D NPS, corrected for lag.[16]

The DQE performance of the prototype MV AMFPI imagers was empirically calculated using the following equation:

$$DQE = \frac{A^2 MTF^2}{\bar{q}_0 NPS}, \tag{1}$$

where A is the average pixel signal, MTF is the presampled MTF, NPS is the empirically determined noise power spectrum, and $\bar{q}_0$ is the mean x-ray fluence ($\sim 8.19 \times 10^6$ photons/mm² for a dose of 1 MU at an SDD of 130 cm).

II.C. Monte Carlo simulations

Empirical MTF and DQE results were compared to those obtained from Monte Carlo simulations of radiation transport, performed using the EGSnrc and DOSXYZnrc codes.[54,55] The methodology for these simulations, detailed in previous publications,[19,22,37] is briefly summarized as follows. The simulated photoconductive detector comprises a layer of HgI₂ (PVD or PIB) coupled with an overlying 1 mm thick Cu plate. The energy absorbed in the HgI₂ was scored as imaging signal. The simulations employed a parallel photon beam with a spectrum corresponding to that of a 6 MV photon beam delivered by a Varian linac.[56] The simulated presampled MTF, MTF_sim, was obtained by simulating energy deposition using a line source with a width of 4 μm and 1×10^8 x-ray histories, with the X rays perpendicularly incident on a detector having a surface area of 40×40 cm².[22,37] The simulated NPS, NPS_sim, was obtained by using a square uniform source (30×30 cm²), with the X rays perpendicularly incident on a detector (consisting of 600×600 pixels with a 508 μm pitch).[37] A total of 100 image frames were simulated with 1×10^9 histories per frame. The signal in the central 500×500 pixels of each frame was used to form ten nonoverlapping slits, each slit consisting of 250×100 pixels. For each slit, after averaging pixel data along the narrower direction, the resulting 250 point realization was detrended and further processed by applying a Hanning window function. The simulated NPS was determined from the average of a series of 1D NPS, obtained from applying Fourier transforms to each of 1000 realizations. The simulated DQE, DQE_sim was determined by means of Eq. (1), using MTF_sim and NPS_sim. Given that only radiation transport was simulated (i.e., not accounting for secondary e-hole pairs created in the photoconductor), the results for MTF_sim and DQE_sim correspond to theoretical upper limits for the prototype imagers.

III. RESULTS

III.A. Selection of electric field strength

Figure 3(a) shows pixel x-ray signal as a function of field strength. Each data point in this figure corresponds to the x-ray signal obtained at a fixed dose from the average of 16 image frames. For each prototype, the signal is seen to increase with increasing field strength before asymptotically approaching a plateau at a field strength of ~0.8 V/μm. Figure 3(b) shows dark current (normalized to unit photoconductor area and obtained using a previously described method)[43] plotted as a function of field strength. For both prototypes, the dark current is seen to increase as field strength increases. However, the PIB prototype exhibits much lower dark current than the PVD prototype. For example, at a field strength of 1 V/μm, the dark current for the PIB prototype (~4 pA/mm²) is ~10 times lower than that of the PVD prototype (~40 pA/mm²). While high dark current consumes pixel signal capacity and leads to large shot noise, the frame times used in the present study were sufficiently short (a maximum of ~330 ms) that neither effect was a consideration in the present investigation. (This differs considerably from the situation for the earlier study conducted under diagnostic conditions where dark current considerations did limit the choice of field strength, with the result that pixel signal extraction for the 20 prototypes was as low as 81%.)[43] Unconstrained by concerns about dark current, the PIB and PVD prototypes were operated at the highest electric field strength that each array would support (~1.3 and ~1.0 V/μm, respectively) without inducing temporal spikes in the dark current. Maximization of the field strengths helped to reduce the known effects of polarization and charge trapping in PIB and PVD detectors[43,44] while also
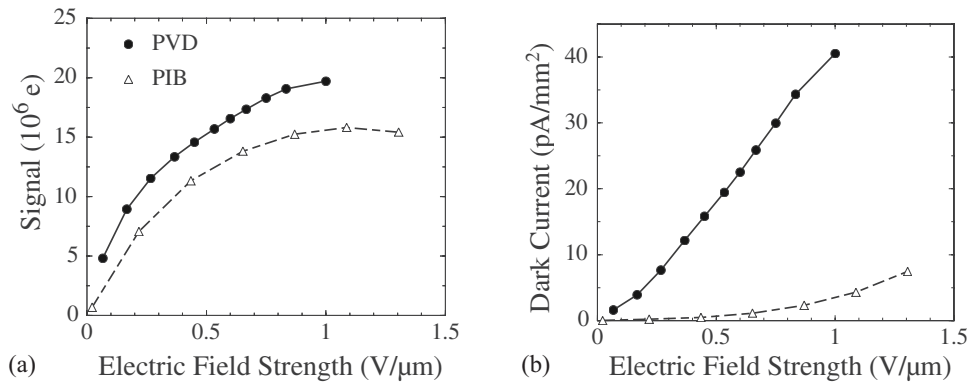
FIG. 3. Measurements from the PIB prototype (open triangles) and the PVD prototype (shaded circles) of (a) x-ray signal response obtained at a fixed dose of ~0.023 MU and (b) dark current. The results are plotted as a function of the electric field strength, calculated from the magnitude of the bias voltage applied across the photoconductor divided by the thickness of the HgI₂ layer.

serving, by virtue of high signal response, to reduce the relative contribution of noise from the acquisition electronics. These field strengths were used for all measurements of sensitivity, lag, MTF, and NPS.

III.B. Sensitivity

Figure 4 shows pixel x-ray signal as a function of dose measured from the PVD and PIB prototypes, as well as from the conventional MV AMFPI. In all cases, pixel signal is seen to increase linearly with increasing dose. The resulting sensitivities (determined from the slopes of these signal response curves) are 855×10^6, 571×10^6, and 310×10^6 e/MU for the PVD, PIB, and conventional MV AMFPI, respectively. The effective work function, W_{eff} (defined as the average amount of absorbed radiation energy required to produce each collected charge), is a metric useful for making valid comparisons of signal collection between detectors. Although all three detectors have similar QE, the conventional MV AMFPI exhibits the lowest sensitivity. For the PVD and PIB prototypes, W_{eff} was determined,[43] using the measured sensitivity and the quantum efficiency given in

Table I, to be 13.8 and 16.9 eV, respectively. These values are lower than that of the FAST B screen (~20.9 eV) obtained from the conventional MV AMFPI.

III.C. Lag

Figure 5 shows pixel signal for a sequence of data frames acquired to determine charge release (i.e., lag) from the PVD prototype. (Similar data, which are not shown, were acquired for the PIB prototype.) Each data point corresponds to the pixel signal relative to a baseline. The baseline is calculated from the pixel signal averaged over the first 30 dark frames (frames #1–30). Signal is seen to increase in an asymptotic manner for the first ~10 image frames (frames #31–40) due to a combination of charge trapping in the detector,[43] as well as the unstable linac output at the beginning of dose delivery. The pixel signal reaches a plateau as the charge trapping and release reach equilibrium and the output of the linac stabilizes. The signal of the last five image frames (frames #246–250) was averaged to provide an equilibrium signal, Q_{EQ}. The signal from data frames following the last image frame
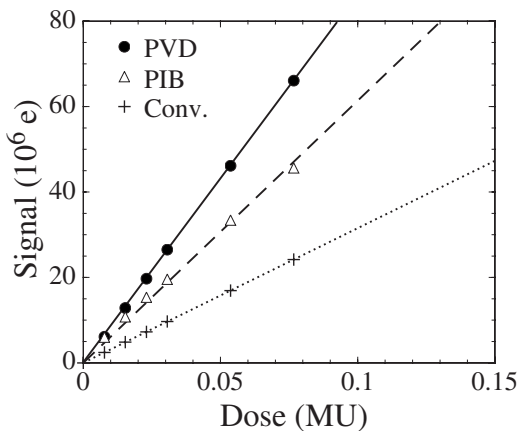

FIG. 4. Pixel signal as a function of dose measured from the PVD and PIB prototypes. For comparison, the signal measured from the conventional MV AMFPI using a Lanex FAST B screen is also presented.
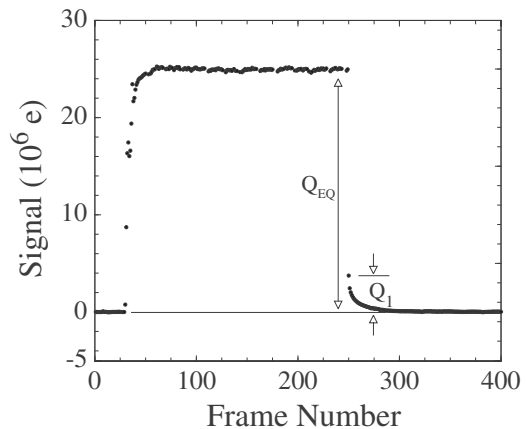

FIG. 5. Pixel signal obtained from the PVD prototype as a function of frame number, illustrating the signals used for lag determination. The data includes 30 dark frames, followed by 220 image frames, and a final 150 dark frames. The dose for each image frame was ~0.031 MU.
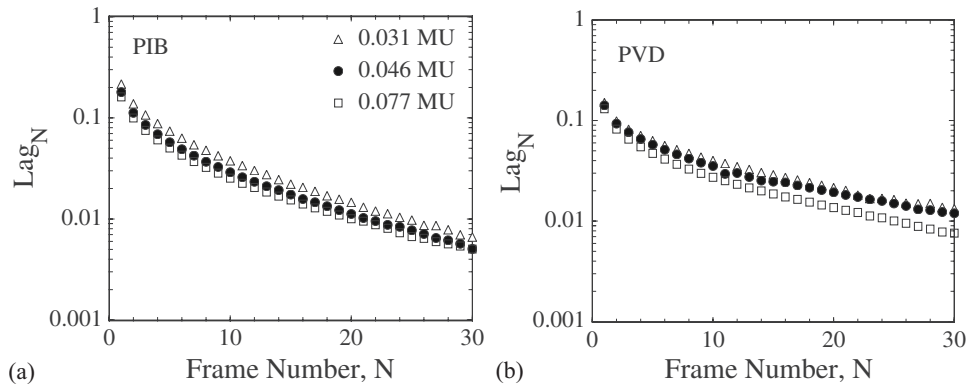
FIG. 6. Lag as a function of frame number, obtained using Eq. (2), for the (a) PIB and (b) PVD prototypes. Results are shown for three different doses.

was used for determination of lag. The lag of the Nth frame after termination of x-ray irradiation, Lag_N, is defined as

$$\mathrm{Lag}_N = \frac{Q_N}{Q_{\mathrm{EQ}}}, \tag{2}$$

where Q_N is the signal of the Nth frame following the last image frame. Figure 6 shows the lag results for the PIB and PVD prototypes. For each prototype, the lag was found to exhibit a weak dependence on dose, slightly decreasing with increasing dose. In addition, the PIB prototype exhibited higher first frame lag ($\mathrm{Lag}_1 \approx 20\%$) than that of the PVD prototype ($\sim 15\%$). Both values are much higher than that exhibited by high quality conventional AMFPIs (typically less than $\sim 5\%$).[57] For subsequent frames, the lag for the PIB prototype decreases faster than that of the PVD prototype. For example, at 0.031 MU, Lag_{30} (obtained ~ 10.5 s after the last image frame) for the PIB prototype is $\sim 0.6\%$ whereas that for the PVD prototype is $\sim 1.3\%$.

III.D. MTF

The presampled MTF results measured from the two prototypes, as well as the corresponding MTF obtained from simulations ($\mathrm{MTF}_{\mathrm{sim}}$) are shown in Fig. 7. The measured and simulated MTF for the PVD prototype are both superior to those for the PIB prototype, due to relatively smaller material thickness and higher material density, leading to reduced lateral spread of radiation in the detector.[22] For both prototypes, the measured MTF is slightly lower than the simulated MTF, $\mathrm{MTF}_{\mathrm{sim}}$. The small difference between measured and simulated MTF is likely due to lateral spreading of the secondary quanta (electrons and holes), an effect that is not accounted for in the simulation. As shown in Fig. 7, the measured MTF results for the PVD and PIB prototypes are higher than that for the conventional MV AMFPI. Given that the phosphor in the conventional MV AMFPI has a thickness and density (i.e., ~ 360 μm and 3.72 g/cm³) that should result in a superior spatial resolution performance (based solely on radiation transport) compared to that for the HgI₂ layer in the PIB prototype (having a thickness of ~ 460 μm and a density of 3.2 g/cm³), the observed inferior resolution

is, most likely, largely due to more pronounced lateral spreading of secondary quanta (optical photons) in the phosphor.[13]

III.E. NPS and DQE

Figure 8 shows the lag-corrected NPS results for the PIB and PVD prototypes. For each prototype, the NPS is observed to increase approximately in proportion to dose, indicating a performance dominated by x-ray quantum noise. In addition, the NPS results exhibit a modest fall off as a function of frequency, indicative of a small degree of pixel-to-pixel noise correlation.

Figure 9 shows measured DQE results from the PIB and PVD prototypes at doses of 0.008, 0.031, and 0.077 MU, along with the DQE results obtained from Monte Carlo simulations. DQE results adapted from published data for the conventional MV AMFPI are also plotted for comparison.[13] For both prototypes, the measured DQE results do not show any obvious dependence on dose, indicating input-quantum-limited behavior starting at the lowest dose of 0.008 MU. In addition, for both prototypes, the measured DQE values are seen to approach the simulation results. The small difference
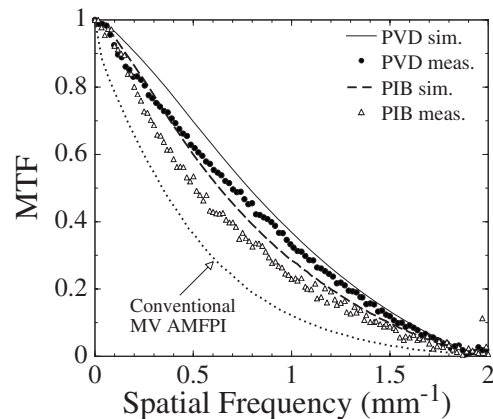

FIG. 7. Presampled MTF measured from the PVD and PIB prototypes. For comparison, simulated MTF results for both prototypes as well as the measured MTF for the conventional MV AMFPI (adapted from data appearing in Ref. 13) are also plotted.
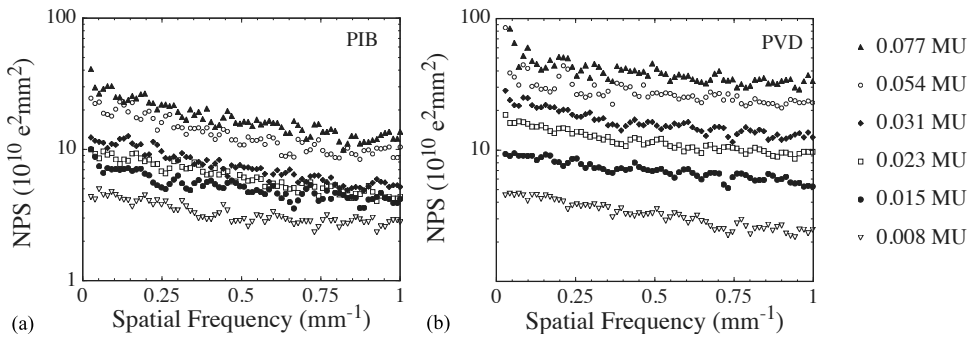
FIG. 8. NPS after lag correction for the (a) PIB and (b) PVD prototypes at six doses.

▲ 0.077 MU
○ 0.054 MU
♦ 0.031 MU
□ 0.023 MU
● 0.015 MU
▽ 0.008 MU

between these measured and simulated DQE results might be due to the aforementioned limitations in the simulation. Moreover, the measured DQE for the prototypes are found to be comparable to, or slightly higher than, that of the conventional MV AMFPI.

IV. SUMMARY AND DISCUSSION

Direct detection, active matrix flat panel imagers based on polycrystalline HgI₂ detectors represent an interesting possibility for significant enhancement in DQE beyond the performance offered by present, conventional MV AMFPIs based on phosphor screens. The attractiveness of polycrystalline HgI₂ approach derives from a combination of the high atomic number and density of polycrystalline HgI₂, the limited spatial spreading of secondary quanta in the material (leading to higher spatial resolution compared to phosphors), and the modest electric field strength necessary for efficient charge collection (~ 1 V/μm as opposed to ~ 10 V/μm for a-Se). While the detector thicknesses of the early PIB and PVD MV AMFPI prototypes reported in this paper provide reasonably high efficiency at diagnostic x-ray energies, they are insufficient to increase x-ray quantum efficiency at radiotherapy energies compared to that provided by conventional MV AMFPIs. Rather, the reported results obtained under radiotherapy conditions serve to provide insight as to the suitability of the approach in general, and to the comparative advantages of the two forms of the material in particular.

In terms of basic pixel properties, the prototypes demonstrated varying degrees of favorable performance. While the PIB prototype exhibited a comparatively low dark current of ~ 4 pA/mm², the PVD prototype showed a value an order of magnitude higher, ~ 40 pA/mm², at an electric field strength of 1 V/μm. As the dominant source of dark signal is believed to be leakage current arising from bulk effects in the photoconductor, it is possible that thicker layers will result in even higher dark current. However, although the limit on dark current for acceptable performance for direct and indirect detection AMFPIs is generally considered to be ~ 10 pA/mm²,[57] the situation is more nuanced in the present case. The relatively low W_{eff} values exhibited by the PIB and PVD prototypes imply that pixel saturation will occur at lower x-ray doses than for conventional MV AMFPIs. (Note that the light emitted from conventional MV AMFPI screens is commonly attenuated through insertion of a neutral density filter so as to extend the range of operation. For a direct detection MV AMFPI, this signal attenuation technique is not available and, while signal could, in principle, be reduced by operating at a lower field strength, this would, in practice, tend to increase undesirable polarization and trapping effects.) Thus, for a given dose rate, MV AMFPIs based on polycrystalline HgI₂ would be operated over shorter pixel integration times to avoid approaching or reaching saturation. Moreover, thicker layers of PIB or PVD will stop a greater fraction of the incident radiation, and perhaps gener-
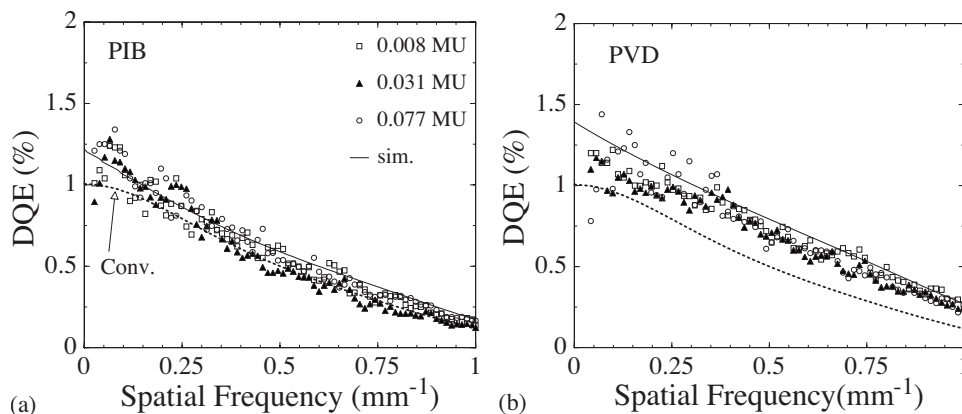

FIG. 9. DQE measured from the (a) PIB and (b) PVD prototypes. For comparison, simulated results for the PIB and PVD prototypes, as well as measured DQE from the conventional MV AMFPI at 1 MU (adapted from data appearing in Ref. 13) are also plotted.

ate even larger pixel signals per beam pulse — further encouraging short integration times. Shorter integration times, in turn, make the imaging system tolerant of high dark currents — with the present PVD prototype operating at a small fraction of pixel saturation and exhibiting good DQE performance in this study, despite its elevated dark current. In brief, barring unexpectedly large (e.g., order of magnitude) increases in dark current compared to the levels observed in the present study, dark current considerations are not expected to favor either PIB or PVD for the MV application. In the case of lag, both prototypes exhibited values of first frame lag (20% and 15% for the PIB and PVD prototypes, respectively) that are much higher than the values of less than ~5% typically exhibited by conventional AMFPIs.[57] The presence of such high levels of lag is likely to intensify undesirable image artifacts such as ghosting and memory and thus degrade fluoroscopic image quality. Therefore, a reduction in the amount of image lag (and in the corresponding trapping of charge) in the photoconductor is required to improve prospects for practical use of devices based on polycrystalline HgI₂. Given that the barrier layer used to protect the surface of the uncoated AMFPI array from the highly reactive HgI₂ may play a significant role in causing charge trapping (as suggested by previously observed polarization effects),[43] further development of promising combinations of the choice of material, thickness, and conductivity of the barrier layer may be key to reducing such effects.

MTF results obtained from the two HgI₂ prototypes indicate superior spatial resolution performance compared to that from the conventional MV AMFPI. While such performance is slightly lower than that expected from radiation transport simulations (indicating the presence of some degree of spatial spreading of secondary quanta in the photoconductor), it nevertheless suggests that thicker layers of HgI₂ could be manufactured without causing prohibitive degradation of spatial resolution.

The effective work function values obtained from the prototypes at 6 MV (~16.9 and 13.8 eV for PIB and PVD, respectively) were found to be much higher than that expected from the single crystal form of HgI₂ (4.2 eV). While this result is parallel to that previously observed at diagnostic x-ray energies,[43] the 6 MV PIB and PVD values are, curiously, also lower and higher than the corresponding diagnostic values (~25 and 11 eV, respectively).[43] The origin of this unexpected behavior is not understood but certainly highlights that the very different composition of the PIB material compared to that of the PVD material (see Fig. 1) results in strongly differing trends in signal collection at MV energies compared to those at diagnostic energies. In any case, these megavoltage W_{eff} values, which are lower than that of the phosphor screens used in conventional MV AMFPIs, provided sufficient signal that the DQE for both prototypes was found to be independent of dose, even down to an extremely low dose of ~0.008 MU corresponding to a single beam pulse. This behavior is indicative of input-quantum-limited operation, a highly desirable characteristic. Furthermore, the DQE performance of the PIB and PVD prototypes (which were similar to and slightly higher than that of the conven-

tional MV AMFPI, respectively) were found to be consistent with predictions obtained from simulation of radiation transport within the photoconductor. Thus, while the DQE from these early prototypes is limited by the relatively modest thickness of the photoconductive layer (providing an x-ray quantum efficiency of ~2.1% and 2.5% for the PIB and PVD prototypes, respectively), the consistency between theoretical expectations and empirical results encourages the idea that considerably thicker detectors will significantly enhance DQE.

It is worthwhile to note that the relatively high signal levels provided by polycrystalline material under MV conditions allow for the possibility of sacrificing some degree of sensitivity in order to improve some other property. For example, early studies suggest that decreasing the grain size of HgI₂ used in the fabrication of the PIB material improves spatial resolution, but at the cost of sensitivity.

While the current study does not identify a clear, performance-related reason to choose between the two forms of polycrystalline HgI₂ examined for the MV application, a non-performance-related consideration (suggested in an earlier publication)[43] possibly favoring the use of PIB over PVD relates to their respective methods of fabrication. The creation of the PVD form of the material takes place in a vacuum vessel and is a relatively slow process with a duration that is in direct proportion to the desired coating thickness. In addition, following deposition, clean-up of the vessel in preparation for further use is very time consuming. Moreover, a large fraction of the relatively expensive HgI₂ material ends up on the vessel walls and is wasted. By comparison, preparation of PIB does not involve deposition in a vessel, the time to fabricate a layer of material is shorter and only weakly related to the thickness of the layer, and virtually all of the HgI₂ material used in the process ends up coated on the array. For that reason, only the PIB form of the material is being pursued in our current research.

Significant improvement in the DQE of MV AMFPIs through development of detectors based on polycrystalline HgI₂ will require further efforts to address the issue of lag discussed above, and the issues of polarization and pixel-to-pixel signal variations noted in a previous study,[43] as well as to realize much thicker, high quality films. The incentive for surmounting these challenges is strong and illustrative examples of the potential performance gains to be achieved appear in Fig. 10. These examples were obtained using Monte Carlo simulation of radiation transport for PIB thicknesses ranging from 2 to 6 mm. 2 mm approximately corresponds to the largest polycrystalline thickness thus far reported[39] and it is anticipated that thicker layers could be created through repeated deposition of PIB layers, allowing each successive layer to fully cure prior to the fabrication of the next layer. The MTFs shown in Fig. 10(a) suggest that spatial resolution degrades slightly with increasing photoconductor thickness, but remains superior to that obtained from the conventional MV AMFPI. Of course, further degradation caused by spatial spreading of secondary quanta, which is not accounted for in these simulations, may further decrease spatial resolution, but is not expected to be signifi-
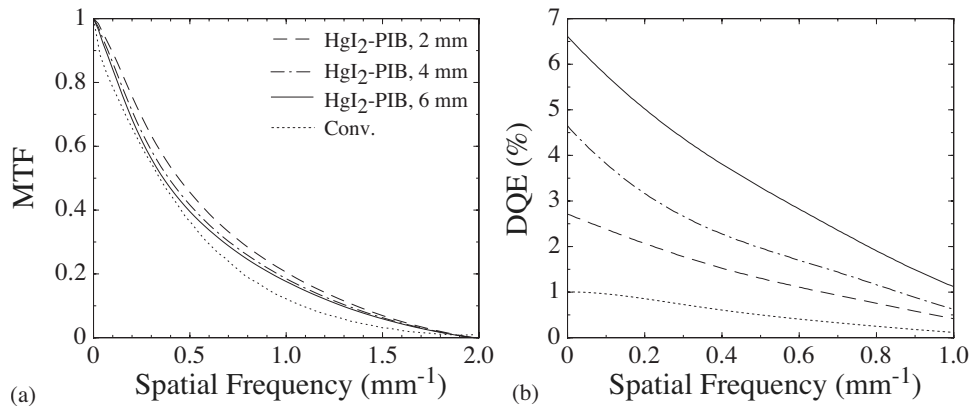
FIG. 10. (a) MTF and (b) DQE for hypothetical direct detection MV AMFPIs with PIB HgI₂ thicknesses of 2, 4, and 6 mm. The MTF and DQE values are derived from results based on Monte Carlo simulations of radiation transport of the type described in Sec. II C, assuming an array pitch of 508 μm and a packing density of 50% (similar to that achieved on the present PIB prototype). For comparison, the measured MTF and DQE from the conventional MV AMFPI are also plotted in (a) and (b), respectively.

cant. The DQEs shown in Fig. 10(b) suggest a significant increase with increasing photoconductor thickness, primarily due to the increase in x-ray quantum efficiency. For example, for a 6 mm thick PIB photoconductor (with a QE of ∼14%), DQE is as high as ∼6.7% — about six times higher than that of the conventional MV AMFPI. The realization of MV AM-FPIs based on thick HgI₂ photoconductors and exhibiting such performance would greatly benefit portal imaging and help improve dose efficiency for advanced MV imaging techniques such as cone beam CT for soft-tissue visualization.

ACKNOWLEDGMENTS

a)Author to whom correspondence should be addressed. Electronic mail: qizhao@umich.edu; Telephone: (734) 763-2154; Fax (734) 763-1369.

b)Present address: Department of Radiation Oncology, Massachusetts General Hospital, Harvard Medical School, Boston, Massachusetts 02114.

c)Present address: Department of Radiation Oncology, 985721 Nebraska Medical Center, Omaha, Nebraska 68198.

d)Present address: Department of Radiation Oncology, Stanford University, Stanford, California 94305.

e)Present address: University of Florida Proton Therapy Institute, Jacksonville, Florida 32206.

f)Present address: Microsoft Corporation, One Microsoft Way, Redmond, Washington 98052.

[1]R. W. Byhardt, J. D. Cox, A. Hornburg, and G. Liermann, "Weekly localization films and detection of field placement errors," Int. J. Radiat. Oncol., Biol., Phys. **4**, 881–887 (1978).

[2]A. L. Boyer, L. E. Antonuk, A. Fenster, M. Van Herk, H. Meertens, P. Munro, L. E. Reinstein, and J. Wong, "A review of electronic portal imaging devices (EPIDs)," Med. Phys. **19**, 1–16 (1992).

[3]J. J. Kruse, M. G. Herman, C. R. Hagness, B. J. Davis, Y. I. Garces, M. G. Haddock, K. R. Olivier, S. L. Stafford, and T. M. Pisansky, "Electronic and film portal images: A comparison of landmark visibility and review accuracy," Int. J. Radiat. Oncol., Biol., Phys. **54**, 584–591 (2002).

[4]L. E. Antonuk, "Electronic portal imaging devices: A review and historical perspective of contemporary technologies and research," Phys. Med. Biol. **47**, R31–R65 (2002).

[5]L. E. Antonuk, Y. El-Mohri, W. Huang, K.-W. Jee, J. H. Siewerdsen, M. Maolinbay, V. E. Scarpine, H. Sandler, and J. Yorkston, "Initial performance evaluation of an indirect-detection, active matrix flat-panel imager

(AMFPI) prototype for megavoltage imaging," Int. J. Radiat. Oncol., Biol., Phys. **42**, 437–454 (1998).

[6]J. Pouliot, M. Aubin, C. Chuang, B. Pickett, M. Roach, and L. Verhey, "Clinical use of an a-Si flat panel for megavoltage portal imaging at UCSF," Med. Phys. **28**, 1218 (2001).

[7]D. G. Drake, D. A. Jaffray, and J. W. Wong, "A prototype amorphous silicon array based radiotherapy portal imager," Proc. SPIE **3032**, 32–41 (1997).

[8]J. Pouliot, A. Bani-Hashemi, J. Chen, M. Svatos, F. Ghelmansarai, M. Mitschke, M. Aubin, P. Xia, O. Morin, K. Bucci, M. Roach III, P. Hernandez, Z. Zheng, D. Hristov, and L. Verhey, "Low-dose megavoltage cone-beam CT for radiation therapy," Phys. Med. Biol. **61**, 552–560 (2005).

[9]T. Falco, H. Wang, and B. G. Fallone, "Preliminary study of a metal/a-Se-based portal detector," Med. Phys. **25**, 814–823 (1998).

[10]M. Lachaîne and B. G. Fallone, "Monte Carlo detective quantum efficiency and scatter studies of a metal/a-Se portal detector," Med. Phys. **25**, 1186–1194 (1998).

[11]G. Pang, D. L. Lee, and J. A. Rowlands, "Investigation of a direct conversion flat panel imager for portal imaging," Med. Phys. **28**, 2121–2128 (2001).

[12]M. Lachaine, E. Fourkal, and B. G. Fallone, "Detective quantum efficiency of a direct-detection active matrix flat panel imager at megavoltage energies," Med. Phys. **28**, 1364–1372 (2001).

[13]Y. El-Mohri, K.-W. Jee, L. E. Antonuk, M. Maolinbay, and Q. Zhao, "Determination of the detective quantum efficiency of a prototype, megavoltage indirect detection, active matrix flat-panel imager," Med. Phys. **28**, 2538–2550 (2001); "Erratum: Strategies to improve the signal and noise performance of active matrix, flat-panel imagers for diagnostic x-ray application," Med. Phys. **33**, 251 (2006).

[14]P. Munro and D. C. Bouius, "X-ray quantum limited portal imaging using amorphous silicon flat-panel arrays," Med. Phys. **25**, 689–702 (1998).

[15]L. E. Antonuk, K.-W. Jee, Y. El-Mohri, M. Maolinbay, S. Nassif, X. Rong, Q. Zhao, J. H. Siewerdsen, R. A. Street, and K. S. Shah, "Strategies to improve the signal and noise performance of active matrix, flat-panel imagers for diagnostic x-ray applications," Med. Phys. **27**, 289–306 (2000).

[16]P. R. Granfors, R. Aufrichtig, G. E. Possin, B. W. Giambattista, Z. S. Huang, J. Liu, and B. Ma, "Performance of a 41×41 cm² amorphous silicon flat panel x-ray detector designed for angiographic and R&F imaging applications," Med. Phys. **30**, 2715–2726 (2003).

[17]Y. El-Mohri, L. E. Antonuk, Q. Zhao, Y. Wang, Y. Li, H. Du, and A. Sawant, "Performance of a high fill factor, indirect detection prototype flat-panel imager for mammography," Med. Phys. **34**, 315–327 (2007).

[18]E. J. Seppi, P. Munro, S. W. Johnsen, E. G. Shapiro, C. Tognina, D. Jones, J. M. Pavkovich, C. Webb, I. Mollov, L. D. Partain, and R. E. Colbeth, "Megavoltage cone-beam computed tomography using a high-efficiency image receptor," Int. J. Radiat. Oncol., Biol., Phys. **55**, 793–803 (2003).

[19]A. Sawant, L. E. Antonuk, Y. El-Mohri, Q. Zhao, Y. Wang, Y. Li, H. Du,

and L. Perna, "Segmented crystalline scintillators: Empirical and theoretical investigation of a high quantum efficiency EPID based on an initial engineering prototype CsI(Tl) detector," Med. Phys. **33**, 1053–1066 (2006).

[20] Y. Wang, L. E. Antonuk, Y. El-Mohri, Q. Zhao, A. Sawant, and H. Du, "Monte Carlo investigations of megavoltage cone-beam CT using thick, segmented scintillating detectors for soft tissue visualization," Med. Phys. **35**, 145–158 (2008).

[21] J.-P. Bissonnette, I. A. Cunningham, and P. Munro, "Optimal phosphor thickness for portal imaging," Med. Phys. **24**, 803–814 (1997).

[22] A. Sawant, L. E. Antonuk, Y. El-Mohri, Y. Li, Z. Su, Y. Wang, J. Yamamoto, Q. Zhao, H. Du, J. Daniel, and R. A. Street, "Segmented phosphors: MEMS-based high quantum efficiency detectors for megavoltage x-ray imaging," Med. Phys. **32**, 553–565 (2005).

[23] E. J. Morton, W. Swindell, D. G. Lewis, and P. M. Evans, "A linear array, scintillation crystal-photodiode detector for megavoltage imaging," Med. Phys. **18**, 681–691 (1991).

[24] J. R. N. Symonds-Tayler, M. Partridge, and P. M. Evans, "An electronic portal imaging device for transit dosimetry," Phys. Med. Biol. **42**, 2273–2283 (1997).

[25] G. Entine, M. R. Squillante, R. Hahn, L. J. Cirignano, W. McGann, and P. J. Biggs, "High contrast, CdTe portal scanner for radiation therapy," IEEE Trans. Nucl. Sci. **39**, 1480–1484 (1992).

[26] D. G. Lewis, W. Swindell, E. J. Morton, P. M. Evans, and Z. R. Xiao, "A megavoltage CT scanner for radiotherapy verification," Phys. Med. Biol. **37**, 1985–1999 (1992).

[27] T. T. Monajemi, D. Tu, B. G. Fallone, and S. Rathee, "A bench-top megavoltage fan-beam CT using CdWO4-photodiode detectors. II. Image performance evaluation," Med. Phys. **33**, 1090–1100 (2006).

[28] H. Keller, M. Glass, R. Hinderer, K. Ruchala, R. Jeraj, G. Olivera, and T. R. Mackie, "Monte Carlo study of a highly efficient gas ionization detector for megavoltage imaging and image-guided radiotherapy," Med. Phys. **29**, 165–175 (2002).

[29] F. DiBianca, S. Samant, J. Laughter, J. Rasmussen, and C. Rodriguez, "Use of a kinestatic charge detector for megavoltage portal imaging," in Proceedings of the SPIE Conference on Physics of Medical Imaging, 1997, Vol. 3032, pp. 195–201.

[30] S. Samant, W. Zheng, F. DiBianca, H. Zeman, and J. Laughter, "A new calibration technique for KCD-based megavoltage imaging," in Proceedings of the SPIE Conference on Physics of Medical Imaging, 1999, Vol. 3659, pp. 779–792.

[31] S. S. Samant and A. Gopal, "Study of a prototype high quantum efficiency thick scintillation crystal video-electronic portal imaging device," Med. Phys. **33**, 2783–2791 (2006).

[32] M. A. Mosleh-Shirazi, P. M. Evans, W. Swindell, J. R. Symonds-Tayler, S. Webb, and M. Partridge, "Rapid portal imaging with a high-efficiency, large field-of-view detector," Med. Phys. **25**, 2333–2346 (1998).

[33] M. A. Mosleh-Shirazi, W. Swindell, and P. M. Evans, "Optimization of the scintillation detector in a combined 3D megavoltage CT scanner and portal imager," Med. Phys. **25**, 1880–1890 (1998).

[34] X. Mei, J. A. Rowlands, and G. Pang, "Electronic portal imaging based on Cerenkov radiation: A new approach and its feasibility," Med. Phys. **33**, 4258–4270 (2006).

[35] G. Pang and J. A. Rowlands, "Development of high quantum efficiency, flat panel, thick detectors for megavoltage x-ray imaging: A novel direct-conversion design and its feasibility," Med. Phys. **31**, 3004–3016 (2004).

[36] F. A. Ghelmansarai, A. Bani-Hashemi, J. Pouliot, E. Calderon, P. Hernandez, M. Mitschke, M. Aubin, and K. Bucci, "Soft tissue visualization using a highly efficient megavoltage cone beam CT imaging system," Proc. SPIE **5745**, 159–170 (2005).

[37] A. Sawant, L. E. Antonuk, Y. El-Mohri, Q. Zhao, Y. Li, Z. Su, Y. Wang, J. Yamamoto, H. Du, I. Cunningham, M. Klugerman, and K. Shah, "Segmented crystalline scintillators: An initial investigation of high quantum efficiency detectors for megavoltage x-ray imaging," Med. Phys. **32**, 3067–3083 (2005).

[38] Y. Wang, L. E. Antonuk, Q. Zhao, Y. El-Mohri, and L. Perna, "High-DQE EPIDs based on thick, segmented BGO and CsI:Tl scintillators: Performance evaluation at extremely low dose," Med. Phys. **36**, 5707–5718 (2009).

[39] M. M. Schieber, H. Hermon, R. A. Street, S. E. Ready, A. Zuck, A. I. Vilensky, L. Melekhov, R. Shatunovsky, M. Lukach, E. Meerson, Y.

Saado, and E. Pinkhasy, "Mercuric iodide thick films for radiological x-ray detectors," in Proceedings of SPIE—Penetrating Radiation Systems and Applications II, 2000, Vol. 4142, pp. 197–204.

[40] M. M. Schieber *et al.*, "Nondestructive imaging with mercuric iodide thick film x-ray detectors," Proc. SPIE **4335**, 43–51 (2001).

[41] G. Zentai *et al.*, "Mercuric iodide and lead iodide x-ray detectors for radiographic and fluoroscopic medical imaging," Proc. SPIE **5030**, 77–91 (2003).

[42] R. A. Street, S. E. Ready, K. Van Schuylenbergh, J. Ho, J. B. Boyce, P. Nylen, K. Shah, L. Melekhov, and H. Hermon, "Comparison of PbI2 and HgI₂ for direct detection active matrix x-ray image sensors," J. Appl. Phys. **91**, 3345–3355 (2002).

[43] H. Du, L. E. Antonuk, Y. El-Mohri, Q. Zhao, Z. Su, J. Yamamoto, and Y. Wang, "Investigation of the signal behavior at diagnostic energies of prototype, direct detection, active matrix, flat-panel imagers incorporating polycrystalline HgI₂," Phys. Med. Biol. **53**, 1325–1351 (2008).

[44] Z. Su, L. E. Antonuk, Y. El-Mohri, L. Hu, H. Du, A. Sawant, Y. Li, Y. Wang, J. Yamamoto, and Q. Zhao, "Systematic investigation of the signal properties of polycrystalline HgI₂ detectors under mammographic, radiographic, fluoroscopic and radiotherapy irradiation conditions," Phys. Med. Biol. **50**, 2907–2928 (2005).

[45] W. Zhao and J. A. Rowlands, "A large area solid-state detector for radiology using amorphous selenium," Proc. SPIE **1651**, 134–143 (1992).

[46] M. M. Schieber, H. Hermon, R. A. Street, S. E. Ready, A. Zuck, A. I. Vilensky, L. Melekhov, R. Shatunovsky, E. Meerson, and Y. Saado, "Radiological x-ray response of polycrystalline mercuric iodide detectors," in Proceedings of SPIE In Medical Imaging 2000: Physics of Medical Imaging, 2000, Vol. 3977, pp. 48–55.

[47] H. Gilboa, A. Zuck, O. Dagan, A. Vilensky, B. N. Breen, A. Taieb, B. Reisman, H. Hermon, G. Zentai, L. Partain, R. Street, and S. Ready, "Medical imaging with mercuric iodide direct digital radiography flat-panel x-ray detectors," in Proceedings of SPIE Conference on the X-Ray and Gamma-Ray Detectors and Applications IV, 2002, Vol. 4784, pp. 315–325.

[48] W. Huang, L. E. Antonuk, J. Berry, M. Maolinbay, C. Martelli, P. Mody, S. Nassif, and M. Yeakey, "An asynchronous, pipelined, electronic acquisition system for active matrix flat-panel imagers (AMFPIs)," Nucl. Instrum. Methods Phys. Res. A **431**, 273–284 (1999).

[49] R. J. Yarema, T. Zimmerman, J. Srage, L. E. Antonuk, J. Berry, W. Huang, and M. Maolinbay, "A programmable, low noise, multichannel ASIC for readout of pixelated amorphous silicon arrays," Nucl. Instrum. Methods Phys. Res. A **439**, 413–417 (2000).

[50] L. E. Antonuk, Y. El-Mohri, J. H. Siewerdsen, J. Yorkston, W. Huang, V. E. Scarpine, and R. A. Street, "Empirical investigation of the signal performance of a high-resolution, indirect detection, active matrix flat-panel imager (AMFPI) for fluoroscopic and radiographic operation," Med. Phys. **24**, 51–70 (1997).

[51] L. E. Antonuk, J. Yorkston, W. Huang, H. Sandler, J. H. Siewerdsen, and Y. El-Mohri, "Megavoltage imaging with a large-area, flat-panel, amorphous silicon imager," Int. J. Radiat. Oncol., Biol., Phys. **36**, 661–672 (1996).

[52] H. Fujita, D. Y. Tsai, T. Itoh, K. Doi, J. Morishita, K. Ueda, and A. Ohtsuka, "A simple method for determining the modulation transfer-function in digital radiography," IEEE Trans. Med. Imaging **11**, 34–39 (1992).

[53] L. E. Antonuk, J. Boudry, W. Huang, D. L. McShan, E. J. Morton, J. Yorkston, M. J. Longo, and R. A. Street, "Demonstration of megavoltage and diagnostic x-ray imaging with hydrogenated amorphous silicon arrays," Med. Phys. **19**, 1455–1466 (1992).

[54] J. A. Treurniet, B. R. B. Walters, and D. W. O. Rogers, "BEAMnrc, DOSXYZnrc, and BEAMDP GUI User's Manual," NRC Report No. PIRS 0623 (Rev B) (2001).

[55] I. Kawrakow and D. W. O. Rogers, "The EGSnrc code system: Monte Carlo simulation of electron and photon transport," Technical Report No. PIRS–701 (National Research Council of Canada, Ottawa, Canada, 2000).

[56] D. Sheikh-Bagheri, Ph.D. thesis, Carleton University, 1999.

[57] L. E. Antonuk, "a-Si:H TFT-based active matrix flat-panel imagers for medical x-ray applications," in *Amorphous Silicon Thin Film Transistors*, Thin Film Transistors, Materials and Processes Vol. 1, edited by Y. Kuo (Kluwer Academic, Boston, 2004), pp. 395–484.